analytical chemistry

pubs.acs.org/ac Article

Catalytic Decomposition of the Hole-Derived H_2O_2 by $AgBiS_2$@Ag Nanozyme to Enhance the Photocurrent of Z-Scheme $BiVO_4/ZnIn_2S_4$ Photoelectrode in Microfluidic Immunosensing Platform

Tingting Wu,[Δ] Xianzhen Song,[Δ] Xiang Ren, Li Dai, Hongmin Ma, Dan Wu, Yuyang Li,* Qin Wei,* and Huangxian Ju

Cite This: *Anal. Chem.* 2022, 94, 12127−12135 Read Online

ACCESS | Metrics & More | Article Recommendations | Supporting Information

ABSTRACT: A novel microfluidic photoelectrochemical (PEC) analytical device based on $AgBiS_2$@Ag nanozyme-mediated signal amplification was developed for ultrasensitive detection of cytokeratin 19 fragment 21−1 (CYFRA 21−1). First, a brand new Z-scheme $BiVO_4/ZnIn_2S_4$ (BZIS) photoactive material was utilized as a sensing matrix to supply a stable photocurrent. Under anodic bias, the photoexcited holes in $BiVO_4$ could oxidize water to produce hydrogen peroxide (H_2O_2), which markedly enhanced the separation efficiency of the electron−hole pairs. Besides, the Z-scheme heterojunction formed between $BiVO_4$ and $ZnIn_2S_4$ further accelerated the transport of the electron. Second, for improving the sensitivity of the PEC sensor, a new strategy of catalytic dissociation of the hole-derived H_2O_2 by $AgBiS_2$@Ag nanozyme was proposed to amplify the PEC signal. $AgBiS_2$@Ag composites, possessing an excellent peroxidase-mimicking feature, could efficiently catalyze the H_2O_2 to produce hydroxyl radicals (•OH) and lead to the significant enhancement of the photocurrent. Third, automatic sample injection and detection were successfully realized by integrating the photoelectrode into microfluidic chips. Based on this advanced sensing strategy, the designed microfluidic PEC sensor displayed a wide linear range (0.1 pg/mL − 100 ng/mL) and a low detection limit of 35 fg/mL (S/N = 3), which could be efficiently applied to the ultrasensitive determination of CYFRA 21−1 in a human serum sample.

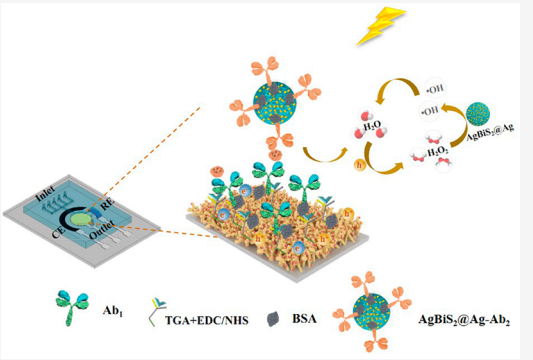

INTRODUCTION

The photoelectrochemical (PEC) sensor, which possesses alluring advantages of low background noise, rapid responses, and high sensitivity, has attracted continuously growing scientific interest in the field of bioanalysis, food analysis, and environmental pollutant monitoring.[1−3] Nevertheless, the lack of miniaturization and portability extremely limits its application in actual sample testing.[4,5] In addition, ultrasensitive and efficient biomarker analysis has great significance for early diagnoses and treatment of disease.[6] Therefore, in this paper, an innovative analytical platform was successfully established, which integrated a microfluidic chip possessing superiorities of less sample consumption, easy integration, and miniaturization with a PEC sensor, and could achieve accurate detection of cytokeratin 19 fragments (CYFRA21−1).

Exploiting photoactive materials with preeminent stability and photocurrent intensity plays an important role in the construction process of a high-performance PEC sensor.[7,8] Nevertheless, traditional photocatalysts such as transition metal oxides, metal sulfide, and perovskite oxides semiconductors have the intrinsic drawbacks of electron transfer tardiness and low light utilization, which inevitably restricts the photoelectric performance of these materials.[9−12] Therefore, it is still urgent to explore photocatalysts with outstanding charge migration capacity and efficient visible-light response. Bismuth vanadate ($BiVO_4$) has aroused great attention due to a moderate band gap (about 2.4 eV) and good chemical stability. Importantly, under anodic bias, the photoexcited holes in $BiVO_4$ can oxidize water to produce H_2O_2, which largely prevented the recombination of electron−hole pairs.[13,14] Meanwhile, $BiVO_4$ with a nanoarray structure shows superior photochemical performances because of the increased specific surface area and active site.[15] However, the high charge recombination of pure $BiVO_4$ seriously hinders its photoactivity. Significantly, Zhao and co-workers have designed a 3-D microsphere Z-scheme $Ag_3VO_4/BiVO_4$ heterojunction and suggested that the visible light absorption and redox ability of the photocatalyst have been vastly enhanced compared to pure

Received: May 20, 2022
Accepted: August 14, 2022
Published: August 23, 2022

https://doi.org/10.1021/acs.analchem.2c02181
Anal. Chem. 2022, 94, 12127−12135

Scheme 1. (A) Preparation Process of Microelectrodes; (B) Fabrication Process of the Microfluidic PEC Sensor; (C) Preparation Process of the $AgBiS_2$@Ag−Ab_2 Bioconjugate

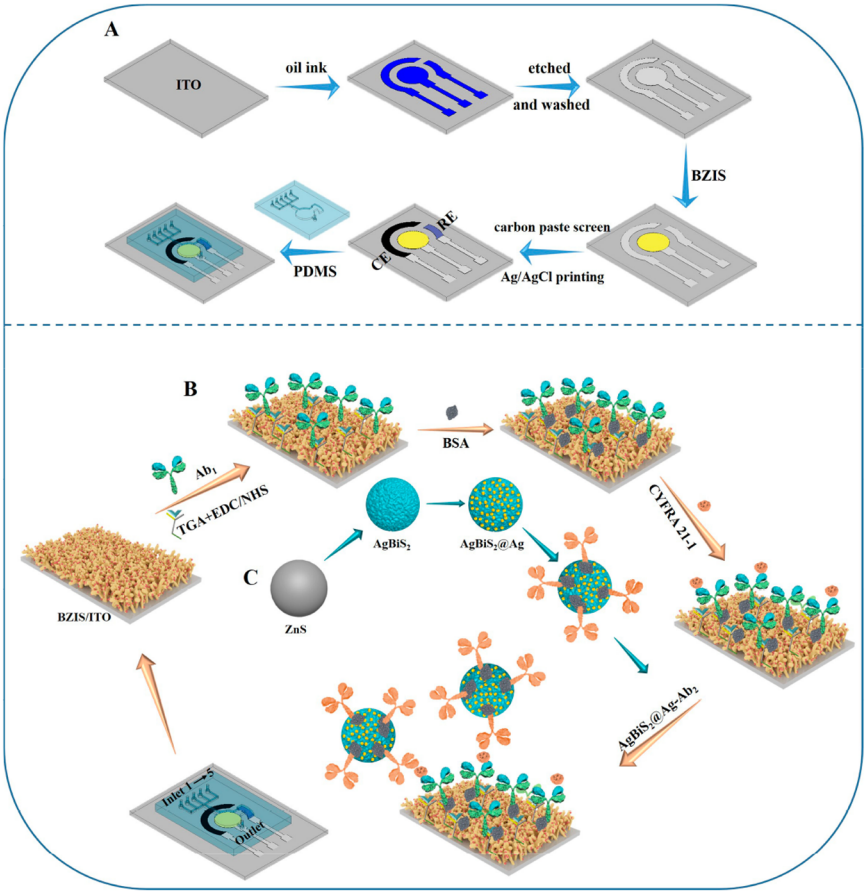

$BiVO_4$.[13] Besides, a diversified $BiVO_4$-based heterojunction such as Z-scheme g-C_3N_4/$BiVO_4$,[16] CdS/$BiVO_4$,[17] $CuFe_2O_4$/$BiVO_4$,[18] and β-Ag_2MoO_4/$BiVO_4$[19] have been triumphantly synthesized and applied to photocatalytic technology. Especially $ZnIn_2S_4$ displayed excellent photoactivity due to its appropriate band structure (∼2.4 eV) and particular electronic and optical properties.[20,21] Inspired by this, in this work, a superior Z-scheme $BiVO_4$/$ZnIn_2S_4$ (BZIS) photoactive material was successfully prepared by decorating the $ZnIn_2S_4$ on the surface of the $BiVO_4$ nanoarray and first utilizing it as a sensing matrix to supply a stable photocurrent.

Moreover, an effective signal amplification strategy is another kernel factor for further improving the sensitivity of the PEC sensor. Among different signal amplification strategies, an enzyme-mediated reaction has become a research hotspot due to its high specificity and catalytic activity, such as biocatalytic precipitation and electron donors/acceptors production.[22−24] Especially nanozymes, combined with the properties of both natural enzymes and nanomaterials, have been widely applied in industrial, medical, and biological fields as an ideal alternative to natural enzymes.[25] Different from the obvious defects of poor stability and rigorous storage conditions of natural enzymes, nanozymes possessed numerous merits, including remarkable catalytic stability, low manufacturing cost, and broad pH.[26−28] It is noteworthy that $AgBiS_2$ as a peroxidase mimic has attracted intensive interest due to its superior enzyme-like activity, which could efficiently catalyze the conversion of H_2O_2 into a reactive oxygen species.[29] Therefore, to vastly accelerate the separation of photocarriers and triumphantly achieve ultrasensitive detection of cytokeratin 19 fragments (CYFRA21−1), a novel strategy of catalytic dissociation of the hole-derived H_2O_2 in BZIS by a $AgBiS_2$@Ag nanozyme for effective consumption of the photogenerated hole was proposed.

Herein, an intriguing microfluidic PEC analytical platform for CYFRA21−1 sensitive determination was designed using detection-antibody (Ab_2)-labeled $AgBiS_2$@Ag as the signal indicator, which could effectively amplify the photocurrent response of the Z-scheme $BiVO_4$/$ZnIn_2S_4$ photoelectrode. First, the Z-scheme heterojunction generated in $BiVO_4$/$ZnIn_2S_4$ composites and the excellent oxidation ability of the holes in $BiVO_4$ toward water evidently increases the electron-transfer rate. Second, the outstanding peroxidase-mimicking feature $AgBiS_2$@Ag nanozyme successfully achieved amplification of the PEC signal. Third, based on the above, a wide linear range (0.1 pg/mL to 100 ng/mL) with a low detection limit of 35 fg/mL was obtained for the precise determination of CYFRA21−1, a biomarker of squamous cell carcinomas chosen as the analyte model, which could verify the satisfied accuracy and practicability of the developed immunosensor.

EXPERIMENTAL SECTION

Wet-Etching of ITO Slices. First, the ITO were cut into 4 × 5 cm^2 sections and cleaned with acetone, ethanol, and ultrapure water each for 0.5 h and dried under nitrogen. Then, to obtain a working (WE) reference (RE) and counter (CE)

https://doi.org/10.1021/acs.analchem.2c02181
Anal. Chem. 2022, 94, 12127−12135

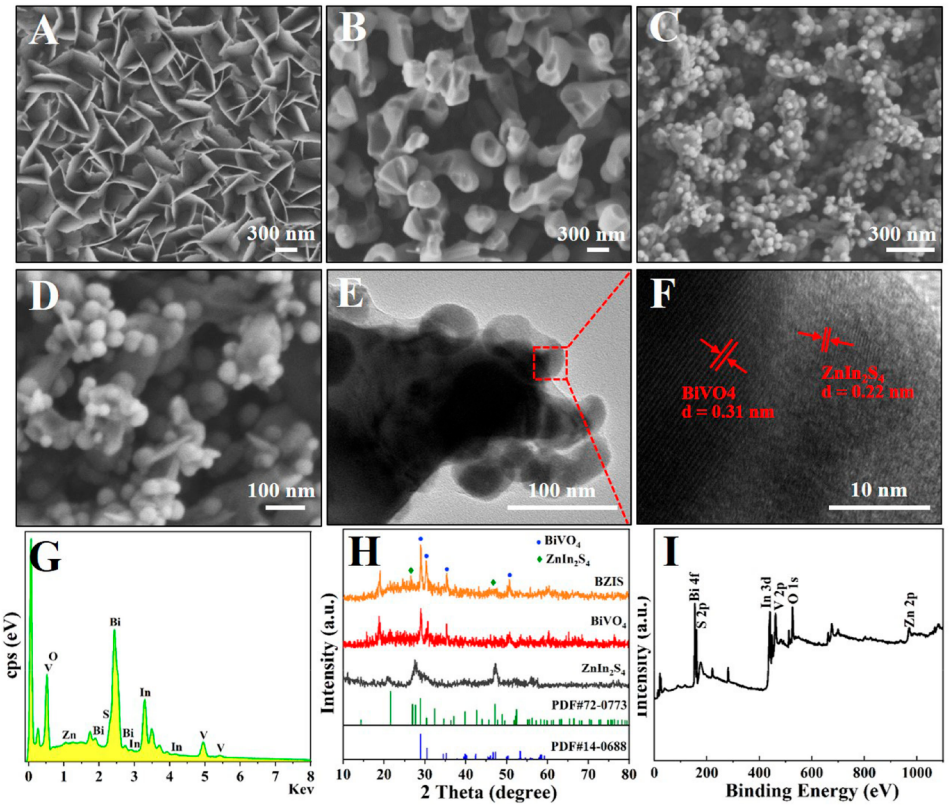

Figure 1. SEM images of (A) BiOI, (B) $BiVO_4$, and (C, D) BZIS; (E) TEM image and (F) HRTEM image of BZIS; (G) EDS spectrum of BZIS; (H) XRD pattern of BZIS; (I) XPS spectra of BZIS.

microelectrodes, the oil ink was printed on ITO by the designed silk-screen mode and dried at 80 °C overnight. Finally, the oil ink-protected ITO substrates were etched (Supporting Information).

Synthesis of $BiVO_4$/$ZnIn_2S_4$ Photoactive Material on Working Microelectrodes. To synthesize the $BiVO_4$ nanoarray, BiOI with a regular thin plate grown on working microelectrodes was first prepared by an electrodeposition procedure (Supporting Information).[14,15] Then BiOI was employed as the precursor to obtain the $BiVO_4$ nanoarray via annealing in air. In detail, 5 μL of 0.2 mol/L $VO(acac)_2$ dissolved in DMSO was added dropwise to the surface of BiOI and dried at room temperature. After that, the modified electrodes were annealed at 450 °C for 2 h (1 °C/min). Finally, 0.1 mol/L NaOH was used to clean the V_2O_5 on the surface of the above electrode.

Z-scheme $BiVO_4$/$ZnIn_2S_4$ (BZIS) photoactive material was prepared through a solvothermal method with minor modifications.[30] Concretely, 0.055 mmol $ZnCl_2$, 0.11 mmol $InCl_3$, and 0.22 mmol thioacetamide were dissolved in 20 mL of ethylene glycol and transferred to a 25 mL Teflon-sealed autoclave. Then a piece of ITO microelectrode, which was decorated with a $BiVO_4$ nanoarray, was immersed into the above mixture. After reacting at 90 °C for 2 h, the microelectrodes were washed with absolute alcohol and dried under vacuum.

Synthesis of $AgBiS_2$@Ag-Ab_2 Bioconjugates. $AgBiS_2$ nanospheres were prepared via a facile polyol process based on ZnS (Supporting Information) as the precursor.[29] In detail, 15 mg of ZnS and 0.6 mg of thiourea were added to 15 mL of ethylene glycol and then stirred for 30 min. Afterward, the solution was transferred to a 50 mL flask and heated to 130 °C for 30 min. Then, 5 mL of ethylene glycol solution containing 22.9 mg of $AgNO_3$ and 65.5 mg of $Bi(NO_3)_3{\cdot}5H_2O$ were added. After 20 min of reaction, the obtained $AgBiS_2$ was washed four times and then dried.

$AgBiS_2$@Ag composites were obtained by a photoassisted reduction method.[31] Typically, 5 mg of $AgBiS_2$ powder and 15 mg of $AgNO_3$ were added into a solution containing 5 mL of ultrapure water and 1 mL of triethanolamine (holes scavenger). Then, the suspension was irradiated under a UV lamp for 2 h to achieve the photoreduction reaction of Ag^+ to Ag nanoparticles. Moreover, $AgBiS_2$@Ag composites were washed thoroughly with ethanol. Subsequently, 1 mL of Ab_2 (10 μg/mL) was added to 1 mL of 3 mg/mL $AgBiS_2$@Ag solution and shaken for 6 h. After washing with PBS, the obtained $AgBiS_2$@Ag−Ab_2 bioconjugates were dispersed into 1 mL of PBS containing 1% BSA (Scheme 1C).

Fabrication Process of the Microfluidic PEC Analytical Platforms. Before the fabrication of the microfluidic PEC sensor, a carbon paste screen and Ag−AgCl conductive ink served as the counter electrode and reference electrode, respectively, which were printed on the ITO microelectrodes. Afterward, the polydimethylsiloxane microfluidic channel obtained from a soft lithography method was attached to the designed three-electrode system by treating with an oxygen plasma treatment for 50 s (Scheme 1A).

The manufacture procedure of the microfluidic PEC sensor for the sensitive determination of CYFRA 21−1 is presented in Scheme 1B. For modifying the hydroxyl group onto the BZIS WE, 15 μL of thioglycolic acid was injected from inlet 1 and held for 1 h. Then, 5 μL of EDC/NHS was also injected from

https://doi.org/10.1021/acs.analchem.2c02181
Anal. Chem. 2022, 94, 12127−12135

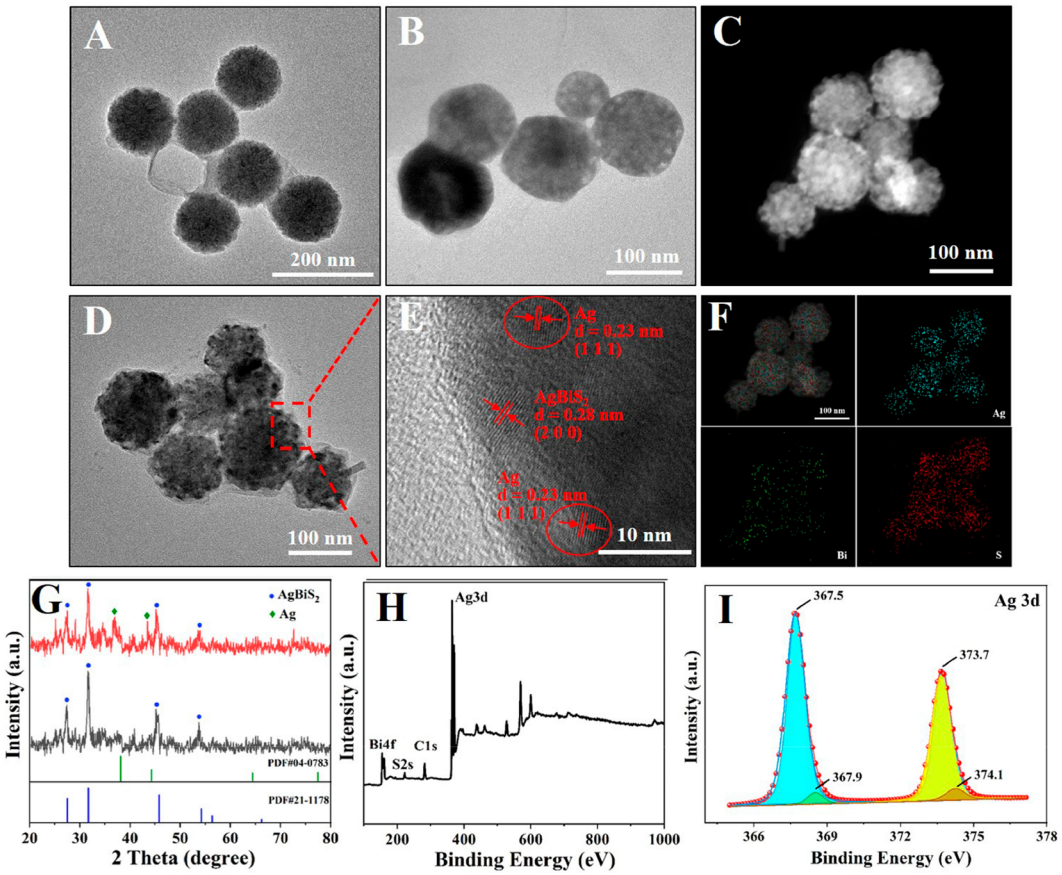

Figure 2. TEM image of (A) ZnS and (B) $AgBiS_2$; (C) STEM and (D) TEM images of $AgBiS_2$@Ag; (E) HRTEM image of $AgBiS_2$@Ag; (F) TEM elemental mapping of $AgBiS_2$@Ag; (G) XRD patterns of $AgBiS_2$ and $AgBiS_2$@Ag; XPS spectra of $AgBiS_2$@Ag (H) composites and XPS high-resolution spectrum of Ag 3d (I).

inlet 1 and held for 30 min to activate the hydroxyl group. Afterward, 15 μL of capture antibody (Ab_1, 1 μg/mL) was injected from inlet 2 and incubated for 1 h. To guarantee the specific interaction of Ab_1 toward CYFRA 21−1, 8 μL of 1% BSA was injected from inlet 3. Finally, unabsorbed species of each step were removed by washing with PBS buffer solution (pH = 7.4).

PEC Analysis of CYFRA 21−1. After passivating the nonspecific binding sites, 15 μL of CYFRA 21−1 (a series of concentrations) was injected from inlet 4, followed with incubating for 1 h. After that, 15 μL of $AgBiS_2$@Ag−Ab_2 bioconjugate was injected from inlet 5 and incubated for 1 h. After rinsing, 150 μL of PBS (pH = 7.0) was injected into the channel of the microfluidic chip. Finally, the photocurrent was measured on an electrochemical workstation (CHI760E) by using a LED lamp (100 mW/cm^2) as the light source, and Figure S1 shows the actual structure of the designed microfluidic biosensor.

RESULTS AND DISCUSSION

Characterization of the $BiVO_4$/$ZnIn_2S_4$ Photoactive Material and $AgBiS_2$@Ag Composites. Z-scheme BZIS composites were successfully prepared to construct the working microelectrodes. Taking BiOI as the template, the $BiVO_4$ nanoarray was obtained through a thermal treatment. Scanning electron microscope (SEM) images were utilized to obtain the morphological information of BiOI, $BiVO_4$, and BZIS. First, in Figure 1A, BiOI displayed a 2D crystal structure with the morphology of a thin plate. After calcination, the plate was converted into a coral-like $BiVO_4$, which owned a large specific surface area (Figure 1B). As shown in the elemental mapping image (Figure S3), only Bi, V, and O elements existed, revealing that BiOI was completely transformed into $BiVO_4$. Second, as the SEM images of BZIS show (Figure 1C,D), large amounts of $ZnIn_2S_4$ nanoparticles with a diameter of 50 nm were uniformly grown on the branch of $BiVO_4$. Meanwhile, the TEM image in Figure 1E,F clearly exhibited the tight coupling between $BiVO_4$ and $ZnIn_2S_4$, and two spacing distances of 0.31 and 0.22 nm observed in Figure 1F were in accordance with the (1 2 1) plans of $BiVO_4$ and the (1 0 0) plans of $ZnIn_2S_4$. In addition, the EDS spectrum (Figure 1G) and elemental mapping image (Figure S4) proved the existence and uniform distribution of Zn, In, and S elements on the $BiVO_4$ nanoarray, which indicated that BZIS was successfully synthesized.

The XRD pattern was used to present the crystal structure of the synthesized BZIS. As depicted in Figure 1H, for the $BiVO_4$ nanoarray, the diffraction peaks at 28.8°, 30.5°, 35.2°, and 50.3° were assigned to the (1 2 1), (0 4 0), (0 0 2), and (2 0 2) facet of the scheelite-monoclinic structure (JCPDS No. 14−0688).[14] After the decoration of $ZnIn_2S_4$, the diffraction peaks of 27.5° and 47.2° matched with the (1 0 2) and (1 1 0) facets of $ZnIn_2S_4$ (JCPDS No. 72−0773) appeared, suggesting the successful preparation of BZIS. Moreover, X-ray photoelectron spectroscopy (XPS) further revealed the atomic bonding states and chemical composition in BZIS. From the survey of the

https://doi.org/10.1021/acs.analchem.2c02181
Anal. Chem. 2022, 94, 12127−12135

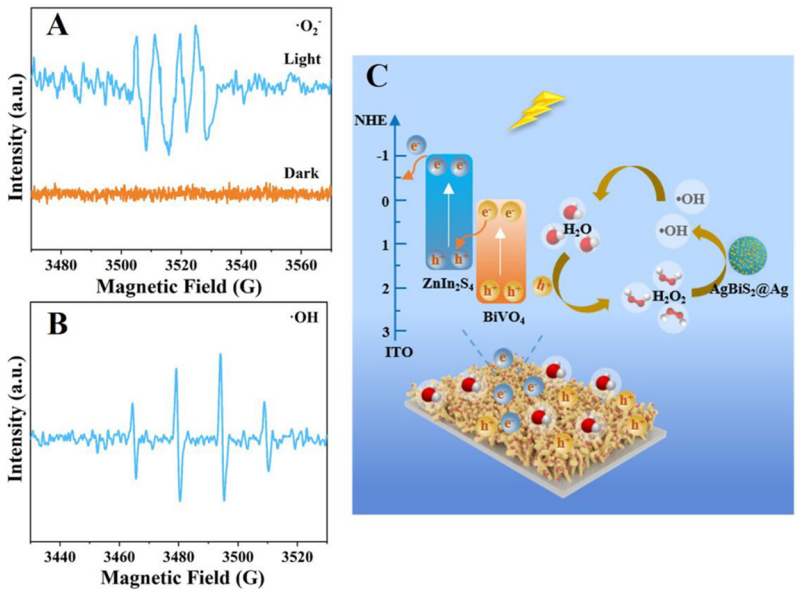

Figure 3. (A) Electronic spin resonance spectra of BZIS composites under dark and visible light: DMPO-$^{\bullet}O^{2-}$; (B) Electronic spin resonance spectra of $AgBiS_2$@Ag nanozyme in the presence of H_2O_2: DMPO − $^{\bullet}OH$; (C) Possible mechanism of the proposed PEC sensing platform.

XPS spectra of BZIS (Figure 1I), the main compositions of Bi, V, O, Zn, In, and S were consistent with the SEM mapping results. The high resolution XPS spectra of each element are shown in the Supporting Information. The XPS results in Figure S5 further confirm the successful coupling of $BiVO_4$ and $ZnIn_2S_4$.

Cyclic voltammetry (CV) was conducted to characterize the variation of the effective electro-active surface area after $ZnIn_2S_4$ decoration. In Figure S6A,B, based on the Randles−Sevcik equation,[32] under scanning rates from 40 to 220 mV/s, the electroactive surface areas were calculated to be 0.44 cm^2 for $BiVO_4$ WE. After $ZnIn_2S_4$ decoration, the electroactive surface area conspicuously increased to 0.54 cm^2, indicating that BZIS composites possess excellent electrochemical activity.

$$I_p = (2.69 \times 10^5)AD^{1/2}n^{3/2}v^{1/2}c$$

$AgBiS_2$@Ag composites were successfully synthesized and serve as a signal label in this work. To obtain $AgBiS_2$ nanospheres, ZnS as a sacrificed template was prepared at first. Figure 2A shows the TEM images of ZnS, and the morphology is nanospheres with a diameter of 100 nm. After cation exchange (Figure 2B), the $AgBiS_2$ retained the shape and size of ZnS, and some pores appeared on the surface of the nanospheres due to the ion exchange process. Moreover, it was found from the STEM image (Figure 2C) and TEM image (Figure 2D) of $AgBiS_2$@Ag composites that the surface of $AgBiS_2$ nanospheres became rough and Ag nanoparticles were uniformly dispersed. As illustrated in the HRTEM images (Figure 2E), the interplanar distances of 0.28 and 0.23 nm were ascribed to the (2 0 0) planes of the $AgBiS_2$ and the (1 1 1) planes of the Ag, respectively, which proved that Ag nanoparticles were tightly grown on $AgBiS_2$ nanospheres, and the TEM elemental mapping further showed that the main elements, including Ag, Bi, and S, homogeneously distributed in the nanospheres, demonstrating the successful preparation of $AgBiS_2$@Ag composites (Figure 2F).

Figure 2G presents the XRD patterns of the $AgBiS_2$ and $AgBiS_2$@Ag composites. The characteristic peaks located at 27.1°, 32.1°, 44.9°, and 54.2° were well matched with the (1 1 1), (2 0 0), (2 2 0), and (3 1 1) planes of $AgBiS_2$ (JCPDS No. 21−1178). For the $AgBiS_2$@Ag composite, two weak diffraction peaks at 37.8° and 44.2° appeared, which belong to (1 1 1) and (2 0 0) facets of Ag (JCPDS No. 04−0783), confirming the presence of Ag nanoparticles in $AgBiS_2$@Ag composite. Furthermore, the XPS spectra of $AgBiS_2$@Ag composites in Figure 2H exhibit the main composition peaks of Ag, Bi, and S, which are matched with the element mapping. As illustrated in Figure 2I, four peaks were observed. Two peaks at 367.5 and 373.7 eV are attributed to Ag $3d_{5/2}$ and Ag $3d_{3/2}$, indicating the existence of Ag^+. Another two peaks located at 367.9 and 374.1 eV could be assigned to metallic Ag, which confirmed that Ag nanoparticles were successfully attached on $AgBiS_2$.[31,33]

Possible Signal Amplification Mechanism of the PEC Sensor. In order to study the photogenerated carriers transfer mechanism, linear sweep voltammetry (LSV) was utilized to determine the conduction band (CB) and valence band (VB) edges of $BiVO_4$ and $ZnIn_2S_4$. As seen in Figure S7A,B, the CB and VB energy levels of $BiVO_4$ were equal to 0 and 2.38 V versus NHE, respectively. The CB and VB energy levels of $ZnIn_2S_4$ in Figure S7C,D were −1 V versus NHE and 1.61 V versus NHE.

Upon visible light irradiation, $BiVO_4$/$ZnIn_2S_4$ composites could produce photoexcited electron−hole pairs (eq 1). First, under normal conditions, the electrons in $ZnIn_2S_4$ may shift to $BiVO_4$; meanwhile, the holes in VB of $BiVO_4$ should inject into $ZnIn_2S_4$, and the reduction potential of O_2/$^{\bullet}O_2^-$ (−0.33 eV) is more negative than the CB of $BiVO_4$, therefore the $^{\bullet}O_2^-$ should not exist in solution. However, the reality is that the electronic spin resonance spectra (ESR) of BZIS composites confirmed the presence of $^{\bullet}O_2^-$ under irradiation (Figure 3A). Consequently, the above results indicated that a Z-scheme heterojunction rather than conventional type II was formed between $BiVO_4$ and $ZnIn_2S_4$. As shown in Figure 3C, the electrons in CB of $BiVO_4$ moved to VB of $ZnIn_2S_4$ and react

https://doi.org/10.1021/acs.analchem.2c02181
Anal. Chem. 2022, 94, 12127−12135

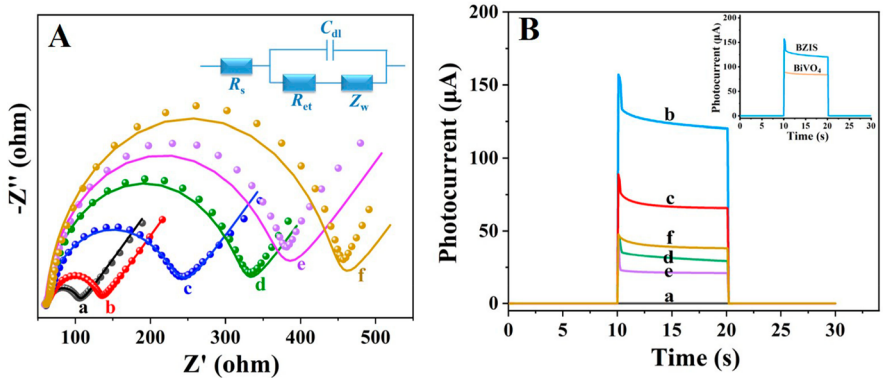

Figure 4. EIS Nyquist plots (A) and photocurrent response of (a) bare WE, (b) BZIS WE, (c) after Ab_1 immobilization, (d) after BSA blocking, (e) after CYFRA 21−1 (0.1 ng/mL), and (f) $AgBiS_2$@Ag−Ab_2 incubation. The illustration is the equivalent circuit (A) and photocurrent of $BiVO_4$ and BZIS (B).

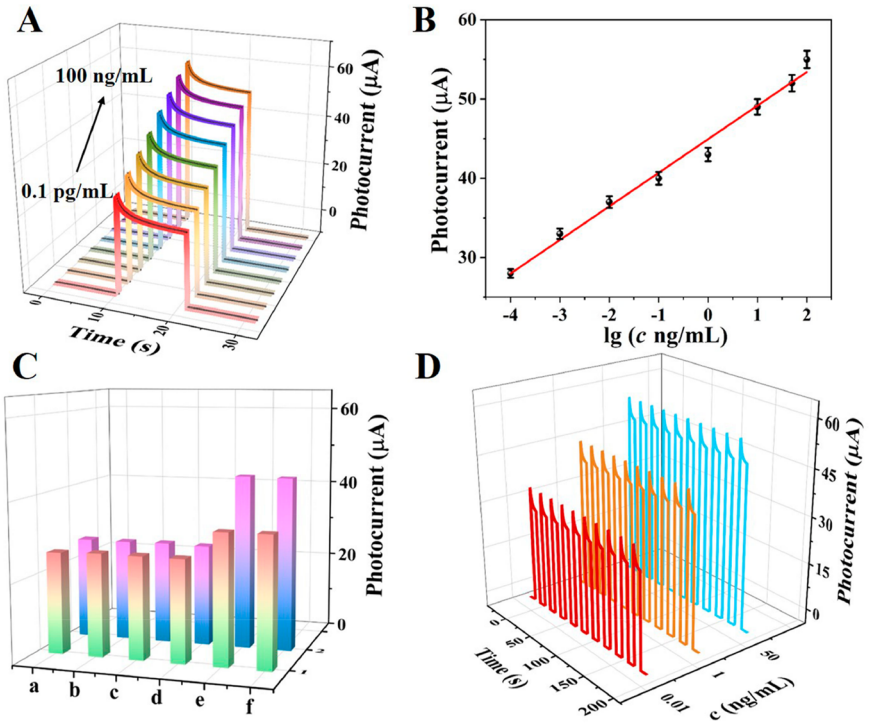

Figure 5. (A) Photocurrent responses with different CYFRA 21−1 concentrations (0.1 pg/mL - 100 ng/mL); (B) Corresponding linear calibration curve; (C) Selectivity of the PEC sensor: (a) blank, (b) PSA, (c) NSE, (d) CEA, (e) CYFRA 21−1, and (f) CYFRA 21−1 + interferences; (D) Stability of the proposed PEC sensor for detecting CYFRA 21−1 (0.01, 1, and 50 ng/mL).

with the photoexcited holes. Simultaneously, the electrons in CB of $ZnIn_2S_4$ transferred to ITO, and the holes in $BiVO_4$ could oxidize water to generate H_2O_2 (eq 2). Second, to further amplify the PEC signal, the $AgBiS_2$@Ag nanozyme was applied to catalyze the produced H_2O_2 in $BiVO_4$. The DMPO spin-trapping ESR spectra in Figure 3B demonstrated the excellent catalytic performance of $AgBiS_2$@Ag toward H_2O_2. When $AgBiS_2$@Ag added to the methanol solutions containing H_2O_2, a strong ESR signal for •OH radical appeared, indicating that H_2O_2 has been catalyzed to produce •OH. Third, the compared experiments were conducted to prove the feasibility of the proposed signal amplification strategy in this work. 3,3′,5,5′-Tetramethylbenzidine (TMB) solution, a reagent that could be oxidized by •OH and produce blue dye products, was promptly added to the PBS solution during PEC measurement in the absence and presence of $AgBiS_2$@Ag. As shown in the Figure S8, in the absence of $AgBiS_2$@Ag, the PBS solution presented faint blues, and the UV−vis absorbance spectroscopy showed a little characteristic peaks of oxidized TMB at 650 nm which could be attributed that few •OH was formed in $BiVO_4$ under anodic bias. In the presence of $AgBiS_2$@Ag, the color immediately became darker and the absorption intensity greatly enhanced, which indicated that the amount of •OH was dramatically increased. The results of compared experiments confirmed that the H_2O_2 was produced by $BiVO_4/ZnIn_2S_4$ and subsequently catalyzed by $AgBiS_2$@Ag nanozyme (eq 3). In this way, more holes could be captured, and the separation efficiency of photoinduced carriers was further improved (Figure 3C).

$$BiVO_4/ZnIn_2S_4 + h\nu \rightarrow h^+ + e^- \quad (1)$$

https://doi.org/10.1021/acs.analchem.2c02181
Anal. Chem. 2022, 94, 12127−12135

$$h^+ + H_2O \rightarrow H_2O_2 \quad (2)$$

$$H_2O_2 \xrightarrow{AgBiS_2@Ag} {}^{\bullet}OH \rightarrow H_2O \quad (3)$$

Characterization of the Modified Process of Microfluidic PEC Sensor. EIS was employed to characterize the interfacial properties of electrodes during each construction step. As shown in Figure 4A, the illustration is the equivalent circuit and the simulated values with ZSimWin software were displayed in Table S1. Bare WE showed a small electron transfer resistance (R_{et}) (curve a), and the R_{et} values become larger when BZIS photoactive material modified on WE (curve b). After the immobilization of Ab_1 (curve c), BSA (curve d), CYFRA 21−1 (curve e), $AgBiS_2$@Ag−Ab_2 (curve f), and R_{et} values orderly increased, proving the successful construction of the microfluidic PEC analytical platform.

The photocurrent response of each step was also recorded to monitor the construction process of the PEC sensor. Figure 4B showed that the coupling of $BiVO_4$ and $ZnIn_2S_4$ achieved about 1.5-fold stronger PEC intensity than that of pure $BiVO_4$ nanoarray. Then, with the incubation of Ab_1 (curve c), BSA (curve d) and CYFRA 21−1 (curve e), the photocurrent gradually declined due to the steric hindrance effect. However, when $AgBiS_2$@Ag-Ab_2 modified, the photocurrent intensity markedly enhanced, which indicated that the PEC sensor has been successfully fabricated.

Analysis of CYFRA 21−1 on the Microfluidic PEC Analytical Device. Under optimal experimental conditions (Figure S9), the novel microfluidic PEC sensor was successfully applied to detect CYFRA 21−1, which had obtained satisfactory results. First, Figure 5A exhibited that with a constant increase of CYFRA 21−1 concentrations, the photocurrent obviously enhanced. Second, in Figure 5B, a good linear correlation was obtained between photocurrent and the logarithm of the CYFRA 21−1 concentration (0.1 pg/mL - 100 ng/mL). The linear fitting equation was $I = 44.932 + 4.237 \lg c$ (ng/mL) and R^2 equaled to 0.987. Simultaneously, the detection limit was 35 fg/mL (S/N = 3), which could guarantee the ultrasensitive analysis of CYFRA 21−1. More importantly, compared to some of the existing detection methods, the proposed PEC sensor presented obvious advantages in sensitive determination of CYFRA 21−1 (Table S2).

Selectivity, stability, and reproducibility were investigated to evaluate the performance of the proposed PEC sensor. First, as illustrated in Figure 5C, PSA, NSE, and CEA were selected as interferences. When only interferences incubated to the modified sensing platform, the photocurrent were closed to blank sample. Meanwhile, when 100-fold of interferences were respectively added to 0.01 and 1 ng/mL CYFRA 21−1, the photocurrent showed slight changes, which indicated that proposed PEC sensor possessed a satisfied selectivity. Then, the stability was evaluated by recording the photocurrent during 10 cycles, as Figure 5D showed, no significant changes were observed which suggested the designed PEC sensor had favorable stability. Besides, the proposed PEC sensor showed satisfactory storage time-based stability (Figure S10). Finally, Figure S11 displayed an excellent reproducibility of the microfluidic PEC sensor.

Real Sample Analysis. The intriguing microfluidic PEC analytical device had effectively realized sensitive determination of CYFRA 21−1 in human serum. Herein, the standard addition method was employed by adding serious concentrations (0.2, 1, and 2 ng/mL) of CYFRA 21−1 to human serum samples (diluted in a 1:10 ratio). As Table S3 shows, the recovery rates are 1.8−3.0% and the RSD is in a range of 99.5−102.0% (n = 5), which reveals that the proposed microfluidic PEC sensor has great potential for CYFRA 21−1 accurate analysis in clinical applications.

CONCLUSIONS

Conclusively, an innovative microfluidic PEC immunosensor based on the photoactive Z-scheme $BiVO_4/ZnIn_2S_4$ as a sensing platform and the $AgBiS_2$@Ag nanozyme as a signal label was first developed for accurate determination of CYFRA 21−1. The outstanding oxidation ability of the photogenerated holes in $BiVO_4$ toward water and well-matched band structure between $BiVO_4$ and $ZnIn_2S_4$ greatly accelerated the separation of photocarriers. To achieve the ultrasensitive detection of CYFRA 21−1, $AgBiS_2$@Ag composites with superb peroxidase-like activity were used to enhance the photocurrent intensity via catalyzing dissociation of the hole-derived H_2O_2. Under optimal conditions, the PEC sensor integrating with the microfluidic chip possessed significant merits of rapid detection and high portability, which showed excellent linearity in the wide range of 0.1 pg/mL to 100 ng/mL and a low detection limit of 35 fg/mL (S/N = 3) for accurate detection of CYFRA 21−1. More importantly, the informative idea of using nanozymes as signal amplifiers provides a new perspective for developing highly efficient PEC sensors for the early diagnosis of diseases.

ASSOCIATED CONTENT

Supporting Information

The Supporting Information is available free of charge at https://pubs.acs.org/doi/10.1021/acs.analchem.2c02181.

Reagents and apparatus, wet-etching of ITO slices, preparation of BiOI nanosheet array, synthesis of ZnS nanospheres, pretreatments of serum sample, actual structure of the designed microfluidic analytical platform, the wavelength range of the stimulation resource, elemental mapping image of $BiVO_4$ and $BiVO_4/ZnIn_2S_4$, XPS spectra of Bi 4f, S 2p, O 1s, V 2p, In 3d and Zn 2p, CV curves and linear relations of electrodes modified with $BiVO_4$ and $BiVO_4/ZnIn_2S_4$, cathodic and anodic linear potential scan for $BiVO_4$ and $ZnIn_2S_4$, UV−vis absorbance spectra and pictures of PBS (containing TMB), optimization of experimental conditions, the storage stability and reproducibility of the proposed PEC sensor, simulation parameters of the equivalent circuit components, comparison of the previously reported methods for CYFRA 21−1 detection, and results of CYFRA 21−1 detection in serum samples by the proposed PEC sensor (PDF)

AUTHOR INFORMATION

Corresponding Authors

Yuyang Li − *Collaborative Innovation Center for Green Chemical Manufacturing and Accurate Detection, Key Laboratory of Chemical Sensing and Analysis in Universities of Shandong, School of Chemistry and Chemical Engineering, University of Jinan, Jinan 250022, China;* orcid.org/0000-0002-1399-9381; Email: chm_liyy@ujn.edu.cn

Qin Wei − *Collaborative Innovation Center for Green Chemical Manufacturing and Accurate Detection, Key*

Laboratory of Chemical Sensing and Analysis in Universities of Shandong, School of Chemistry and Chemical Engineering, University of Jinan, Jinan 250022, China; orcid.org/0000-0002-3034-8046; Phone: +86 531 82765730; Email: sdjndxwq@163.com; Fax: +86 531 82765969

Authors

Tingting Wu − *Collaborative Innovation Center for Green Chemical Manufacturing and Accurate Detection, Key Laboratory of Chemical Sensing and Analysis in Universities of Shandong, School of Chemistry and Chemical Engineering, University of Jinan, Jinan 250022, China*

Xianzhen Song − *Collaborative Innovation Center for Green Chemical Manufacturing and Accurate Detection, Key Laboratory of Chemical Sensing and Analysis in Universities of Shandong, School of Chemistry and Chemical Engineering, University of Jinan, Jinan 250022, China*

Xiang Ren − *Collaborative Innovation Center for Green Chemical Manufacturing and Accurate Detection, Key Laboratory of Chemical Sensing and Analysis in Universities of Shandong, School of Chemistry and Chemical Engineering, University of Jinan, Jinan 250022, China;* orcid.org/0000-0002-4321-4282

Li Dai − *Collaborative Innovation Center for Green Chemical Manufacturing and Accurate Detection, Key Laboratory of Chemical Sensing and Analysis in Universities of Shandong, School of Chemistry and Chemical Engineering, University of Jinan, Jinan 250022, China*

Hongmin Ma − *Collaborative Innovation Center for Green Chemical Manufacturing and Accurate Detection, Key Laboratory of Chemical Sensing and Analysis in Universities of Shandong, School of Chemistry and Chemical Engineering, University of Jinan, Jinan 250022, China;* orcid.org/0000-0002-7061-8944

Dan Wu − *Collaborative Innovation Center for Green Chemical Manufacturing and Accurate Detection, Key Laboratory of Chemical Sensing and Analysis in Universities of Shandong, School of Chemistry and Chemical Engineering, University of Jinan, Jinan 250022, China;* orcid.org/0000-0002-8732-5988

Huangxian Ju − *Collaborative Innovation Center for Green Chemical Manufacturing and Accurate Detection, Key Laboratory of Chemical Sensing and Analysis in Universities of Shandong, School of Chemistry and Chemical Engineering, University of Jinan, Jinan 250022, China; State Key Laboratory of Analytical Chemistry for Life Science, Department of Chemistry, Nanjing University, Nanjing 210023, China;* orcid.org/0000-0002-6741-5302

Complete contact information is available at: https://pubs.acs.org/10.1021/acs.analchem.2c02181

Author Contributions

[Δ]T.T.W. and X.Z.S. contributed equally to this work.

Notes

The authors declare no competing financial interest.

■ ACKNOWLEDGMENTS

This study was supported by the National Key Scientific Instrument and Equipment Development Project of China (No. 21627809), National Natural Science Foundation of China (No. 21777056), Special Foundation for Taishan Scholar Professorship of Shandong Province, Jinan Scientific Research Leader Workshop Project (2018GXRC024, 2018GXRC021), the Innovation Team Project of Colleges and Universities in Jinan (No.2019GXRC027), and the Natural Science Foundation of Shan-dong Province (ZR2020QB097).

■ REFERENCES

(1) Mao, L.; Liu, H.; Yao, L.; Wen, W.; Chen, M. M.; Zhang, X.; Wang, S. *Chem. Eng. J.* **2022**, *429*, 132297.
(2) Hu, J.; Lu, M. J.; Chen, F. Z.; Jia, H. M.; Zhou, H.; Li, K.; Zeng, X.; Zhao, W. W.; Lin, P. *Adv. Funct. Mater.* **2022**, *32*, 2109046.
(3) Zhang, Z.; Liu, Q.; Zhang, M.; You, F.; Hao, N.; Ding, C.; Wang, K. *J. Hazard. Mater.* **2021**, *416*, 125988.
(4) Gao, R.; Lv, Z.; Mao, Y.; Yu, L.; Bi, X.; Xu, S.; Cui, J.; Wu, Y. *ACS Sensors* **2019**, *4* (4), 938−943.
(5) Cheng, Q.; Feng, J.; Wu, T.; Zhang, N.; Wang, X.; Ma, H.; Sun, X.; Wei, Q. *Anal. Chem.* **2021**, *93* (40), 13680−13686.
(6) Du, Y.; Xue, J.; Sun, X.; Wu, D.; Liu, X.; Ju, H.; Yang, L.; Wei, Q. *Anal. Chem.* **2020**, *92* (12), 8472−8479.
(7) Wang, Y.; Liu, Q.; Wei, J.; Dai, Z.; Ding, L.; Yuan, R.; Wen, Z.; Wang, K. *Biosen. Bioelectron.* **2021**, *173*, 112771.
(8) Peng, B.; Zhang, Z.; Tang, L.; Ouyang, X.; Zhu, X.; Chen, L.; Fan, X.; Zhou, Z.; Wang, J. *Analy. Chem.* **2021**, *93* (26), 9129−9138.
(9) Chen, H.; Rim, Y. S.; Wang, I. C.; Li, C.; Zhu, B.; Sun, M.; Goorsky, M. S.; He, X.; Yang, Y. *ACS Nano* **2017**, *11* (5), 4710−4718.
(10) Liang, J.; Chen, D.; Yao, X.; Zhang, K.; Qu, F.; Qin, L.; Huang, Y.; Li, J. *Small* **2020**, *16* (15), 1903398.
(11) Zhang, M.; Li, F.; Benetti, D.; Nechache, R.; Wei, Q.; Qi, X.; Rosei, F. *Nano Energy* **2021**, *81*, 105626.
(12) Li, F.; Zhang, M.; Benetti, D.; Shi, L.; Besteiro, L. V.; Zhang, H.; Liu, J.; Selopal, G. S.; Sun, S.; Wang, Z.; Wei, Q.; Rosei, F. *Appl. Catal., B* **2021**, *280*, 119402.
(13) Zhao, W.; Feng, Y.; Huang, H.; Zhou, P.; Li, J.; Zhang, L.; Dai, B.; Xu, J.; Zhu, F.; Sheng, N.; Leung, D. Y.C. *Appl. Catal., B* **2019**, *245*, 448−458.
(14) Kim, K.; Lee, S. H.; Choi, D. S.; Park, C. B. *Adv. Funct. Mater.* **2018**, *28* (41), 1802813.
(15) Feng, J.; Li, F.; Liu, L.; Liu, X.; Qian, Y.; Ren, X.; Wang, X.; Wei, Q. *Sens. Actuators B Chem.* **2020**, *308*, 127685.
(16) Safaei, J.; Ullah, H.; Mohamed, N. A.; Mohamad Noh, M. F.; Soh, M. F.; Tahir, A. A.; Ahmad Ludin, N.; Ibrahim, M. A.; Wan Isahak, W. N. R.; Mat Teridi, M. A. *Appl. Catal., B* **2018**, *234*, 296−310.
(17) Zhou, F. Q.; Fan, J. C.; Xu, Q. J.; Min, Y. L. *Appl. Catal., B* **2017**, *201*, 77−83.
(18) Chen, M.; Zhao, J.; Huang, X.; Wang, Y.; Xu, Y. *ACS Appl. Mater. Interfaces* **2019**, *11* (49), 45776−45784.
(19) Chen, Y.; Xie, X.; Si, Y.; Wang, P.; Yan, Q. *Appl. Surf. Sci.* **2019**, *498*, 143860.
(20) Hu, J.; Chen, C.; Zheng, Y.; Zhang, G.; Guo, C.; Li, C. M. *Small* **2020**, *16* (37), 2002988.
(21) Yan, T.; Wu, T.; Wei, S.; Wang, H.; Sun, M.; Yan, L.; Wei, Q.; Ju, H. *Biosen. Bioelectron.* **2020**, *148*, 111739.
(22) Chen, G.; Qin, Y.; Jiao, L.; Huang, J.; Wu, Y.; Hu, L.; Gu, W.; Xu, D.; Zhu, C. *Analy. Chem.* **2021**, *93* (17), 6881−6888.
(23) Zhu, J. H.; Gou, H.; Zhao, T.; Mei, L. P.; Wang, A. J.; Feng, J. J. *Biosen. Bioelectron.* **2022**, *203*, 114048.
(24) Zhuang, J.; Han, B.; Liu, W.; Zhou, J.; Liu, K.; Yang, D.; Tang, D. *Biosen. Bioelectron.* **2018**, *99*, 230−236.
(25) Huang, Y.; Ren, J.; Qu, X. *Chem. Rev.* **2019**, *119* (6), 4357−4412.
(26) Wang, H.; Wan, K.; Shi, X. *Adv. Mater.* **2019**, *31* (45), 1805368.
(27) Zhang, P.; Sun, D.; Cho, A.; Weon, S.; Lee, S.; Lee, J.; Han, J. W.; Kim, D. P.; Choi, W. *Nat. Commun.* **2019**, *10* (1), 940.
(28) Zhang, J.; Zhang, X.; Gao, Y.; Yan, J.; Song, W. *Biosen. Bioelectron.* **2021**, *176*, 112945.

(29) Chen, B.; Zhang, C.; Wang, W.; Chu, Z.; Zha, Z.; He, X.; Zhou, W.; Liu, T.; Wang, H.; Qian, H. *ACS Nano* **2020**, *14* (11), 14919−14928.
(30) Han, Q.; Li, L.; Gao, W.; Shen, Y.; Wang, L.; Zhang, Y.; Wang, X.; Shen, Q.; Xiong, Y.; Zhou, Y.; Zou, Z. *ACS Appl. Mater. Interfaces* **2021**, *13* (13), 15092−15100.
(31) Zhang, L.; Feng, L.; Li, P.; Chen, X.; Xu, C.; Zhang, S.; Zhang, A.; Chen, G.; Wang, H. *Chem. Eng. J.* **2021**, *409*, 128154.
(32) Wang, H.; Yuan, Y.; Zhuo, Y.; Chai, Y.; Yuan, R. *Anal. Chem.* **2016**, *88* (4), 2258−2265.
(33) Li, C.; Zhang, A.; Zhang, L.; Song, J.; Su, S.; Sun, Z.; Xiang, J. *Appl. Surf. Sci.* **2018**, *433*, 914−926.

https://doi.org/10.1021/acs.analchem.2c02181
Anal. Chem. 2022, 94, 12127−12135